Journal of Membrane Science 595 (2020) 117502

Contents lists available at ScienceDirect

Journal of Membrane Science

journal homepage: http://www.elsevier.com/locate/memsci

Microstructural effects on permeability of Nitrocellulose membranes for biomedical applications

Shanyouming Sun [a,b,c,e], Shangsheng Feng [c,d,*], Changchun Ji [c,f], Meng Shi [c], Xiaocong He [c,d], Feng Xu [c,d], Tian Jian Lu [b,e,**]

[a] State Key Laboratory for Strength and Vibration of Mechanical Structures, Xi'an Jiaotong University, Xi'an, 710049, PR China
[b] State Key Laboratory of Mechanics and Control of Mechanical Structures, Nanjing University of Aeronautics and Astronautics, Nanjing, 210016, PR China
[c] Bioinspired Engineering and Biomechanics Center (BEBC), Xi'an Jiaotong University, Xi'an, 710049, PR China
[d] The Key Laboratory of Biomedical Information Engineering of Ministry of Education, School of Life Science and Technology, Xi'an Jiaotong University, Xi'an, 710049, PR China
[e] Nanjing Center for Multifunctional Lightweight Materials and Structures (MLMS), Nanjing University of Aeronautics and Astronautics, Nanjing, 210016, PR China
[f] Department of Acupuncture and Moxibustion, Shaanxi Traditional Chinese Medicine Hospital, Xi'an, 710003, PR China

ARTICLE INFO

Keywords:
Wicking flow
Pore morphology
Thin-film porous materials
Paper microfluidics
Lateral flow assay

ABSTRACT

Nitrocellulose membrane (NC), as a paper-like matrix with microscale porous structures, has found widespread applications in biomedical fields due to its excellent biological features and physiochemical properties. In these biomedical applications, diffusion, convection, and binding reaction of biomolecules (e.g., acids and proteins) in NC through wicking flow is the fundamental physical process. However, the optimization of NC based biomedical devices has been limited by the lack of the understanding on the wicking flow behavior of NC membranes from the microstructural point of view. To address this, we experimentally and theoretically investigated the microstructural effects on the wicking flow behaviors (e.g., permeability, effective pore radius) of NC membrane and found that the wicking flow is highly dependent on the pore-morphology characterizing parameters (e.g., porosity and pore size). We further developed a theoretical model yielding a closed-form solution to predict the microstructure-permeability relation, which was validated by our experimental results. Our theoretical model would be a powerful tool for tailoring the wicking flow behavior of NC membranes through controlling the microstructural parameters, and thus for optimizing NC membrane-based biomedical devices from the view point of material design in the future.

1. Introduction

Nitrocellulose (NC) membrane, as a paper-like matrix with microscale porous structures, has found widespread applications in biomedical fields, mainly due to its excellent biocompatibility, unique physiochemical properties (e.g., appropriate pore size, high surface area), and the ability to immobilize various biomolecules (e.g., proteins, nucleic acids) [1]. For instance, NC membrane is commonly used for immobilizing nucleic acids in southern blots and northern blots, and immobilizing proteins in western blots [1]. It is also widely used as substrate materials in various diagnostic devices (e.g., lateral flow assays (LFAs), where NC membrane serves as the reaction surface upon which the critical immunocomplexes form [2]), where antigen-antibody binding or nucleic acid hybridization occurs [3]. In these biomedical applications, diffusion, convection and binding reaction of acids and proteins are the fundamental processes [4], where wicking flow in NC membrane plays a critical role. For instance, the protein transfer (via electrophoretic transfer) in western blots [1] and the transport of nanoparticles in LFAs [5] are both driven and greatly affected by the wicking flow in NC membrane materials. Therefore, it is of great importance to understand and control the wicking flow in NC for these biomedical applications.

The wicking flow in NC membrane and other paper-like porous materials has been extensively studied, mostly from macroscopic point

* Corresponding author. Bioinspired Engineering and Biomechanics Center (BEBC), Xi'an Jiaotong University, Xi'an, 710049, PR China.
** Corresponding author. State Key Laboratory of Mechanics and Control of Mechanical Structures, Nanjing University of Aeronautics and Astronautics, Nanjing, 210016, PR China.
E-mail addresses: shangshengfeng@xjtu.edu.cn (S. Feng), tjlu@nuaa.edu.cn (T.J. Lu).

https://doi.org/10.1016/j.memsci.2019.117502
Received 11 July 2019; Received in revised form 19 September 2019; Accepted 22 September 2019
Available online 23 September 2019
0376-7388/© 2019 Elsevier B.V. All rights reserved.

of view [6–15]. For instance, Elizalde et al. [6] proposed a fluid dynamics model for homogeneous porous paper with arbitrary cross-sectional shapes, which enables determining the cross-sectional profile required for a prescribed fluid velocity or mass transport rate. Fu and coworkers [7–9] developed the electrical circuit analogy of fluid flow through a porous channel to predict mass flow rate distributions in paper network. Effects of evaporation on the wicking dynamics in the filter papers for paper-based diagnostics were experimentally and numerically studied by Liu et al. [10]. Böhm et al. [16] summarized recent advances and outlined design strategies for successful microfluidic paper-based applications. Chaudhury et al. [17] proposed a generalization in the pertinent diffusive dynamics to understand and control capillary-driven transport of a fluid within the complex porous matrix of paper. Based on these macroscopic models as mentioned above, various methods have been developed for controlling fluid flow and reagent transport in LFAs and paper-based analytical devices by creating hydrophobic barriers such as wax [11,12] or polymer [18], alteration of the geometry of the paper network [13], or integration of fluidic valve in the flow channel [14,15]. However, existing studies were limited to modeling and controlling the wicking flow at the macroscale, thus could not be used in the material design of NC by considering the microstructural effects.

NC membrane has a complicated three-dimensional (3D) microstructure which looks like inter-connected particles arranged in a 3D matrix. Actually, the microstructure of a porous material has been found to have significant effect on the pore-scale flow [19,20] and diffusion [21] behavior, and thus on the reagent dispersion, mixing and chemical reaction within the porous structure, which is commonly to see in chemical engineering [22,23] and biomedical applications [24]. In particular, in case of diffusion-limited reactions the flow transport dominates the whole physiochemical process, e.g., the antigen-antibody binding reactions in the shear flow [4]. Therefore, the microstructure of a porous material serving as the reaction bed plays a significant role in determining the overall performance of biochemical reactors [22–24]. Although microstructural effects of paper have been studied extensively using various high-end technologies such as space and time-resolved confocal fluorescence microscopy [25,26], the microstructural effects on the wicking flow and transport in NC membranes with unique pore morphology have not been explored yet.

The flow permeability is an important fluid mechanical property that determines the wicking flow behavior in porous materials [27], which relies only on the microstructure of porous materials themselves [27]. The microstructure-permeability relationship have been widely explored for the two common types of porous materials: the granular and foam matrix materials. For instance, the well-known Blake-Kozeny model [28] has been the most famous formulation to determine the permeability of granular materials usually with a low porosity (<0.5). Byon et al. [19,29] investigated the effect of particle size distribution and packing structure on the permeability of sintered porous wicks. Based on three representative types of particle arrangements, Ngo et al. [30] investigated the permeability of microporous wicks with geometric inverse to sintered particles. Recently, Zhang et al. [27] correlated the permeability of microporous copper structures fabricated using template-assisted electrodeposition with neck diameter, porosity, and pore diameter. As the microstructure of matrix porous materials differs from the granular materials, the models for granular type failed to predict the permeability of the matrix materials. Consequently, specific models have been developed based on the microstructure of matrix materials, including the classic tetrakaidecahedron model [31], the cubic cell model [32,33], the Kelvin's model [20], as well as the W–P model [34] with minimized surface area. As shown in Fig. 1, the microstructure of NC membrane is obviously different from the granular and matrix porous materials, which nevertheless, can be viewed as a hybrid of the latter two. The existing models built for the granular and the matrix materials could not predict the permeability of NC membrane accurately.

In this study, we aim to explore the microstructural effects on the capillary flow behavior of NC membrane with a focus on its microstructure-permeability relationship. First, we characterized the pore microstructure of NC membrane by measuring its particle/pore size distributions and porosity. Then, we measured the permeability and effective pore radius of NC membranes with different microstructures through capillary flow experiments. Subsequently, we proposed a geometrical model (e.g., particle-cubic unit cell model) to represent the pore morphology of NC membrane. Based on the idealized unit cell model, the permeability of NC membrane was numerically and theoretically modeled as a function of pore microstructural parameters. Finally, we discussed effects of the microstructure on the capillary flow behavior of NC membrane. Our theoretical model would be a powerful tool for tailoring the wicking flow behavior of NC membranes through controlling the microstructural parameters, and thus for optimizing NC membrane-based biomedical devices from the view point of material design in the future.

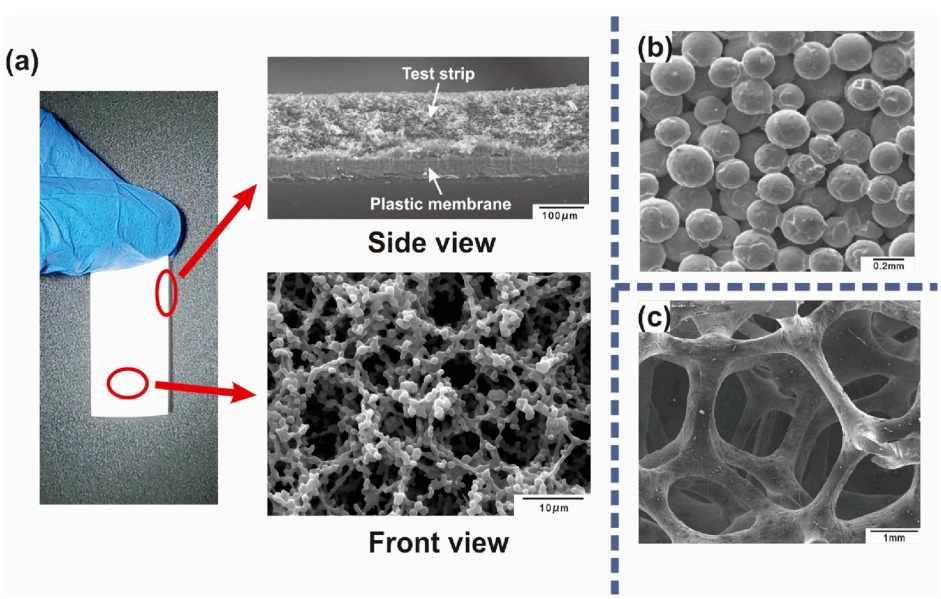

Fig. 1. The microstructures of several representative porous materials. (a) NC membrane; (b) sintered granular media [48]; (c) metal foam matrix.

2. Materials and methods

2.1. Pore structure characterization

Porosity. Common methods for measuring the porosity of a porous medium include mercury-intrusion porosimetry [35], nitrogen adsorption [36] and weighting method [37]. Since mercury-intrusion porosimetry relies on external pressure to overcome surface tension of mercury being pressed into the pore of the membrane, which may destroy the pore structure of NC membrane due to its brittleness, it is not feasible to measure the porosity using this method. On the other hand, nitrogen adsorption is often used to characterize pore size distributions of micropores and mesopores with diameters below 2 nm and 50 nm, respectively [38], thus not suitable for NC membranes typically having pore diameters exceeding 1 μm as well. Therefore, in the present study, the weighting method was employed to measure the porosity of NC membranes. The porosity ε is defined as:

$$\varepsilon = \frac{V_{pore}}{V} = \frac{m_b - m_a}{\rho \cdot V} \tag{1}$$

where V_{pore} is the pore volume, V is the sample volume. m_a is the dry weight of sample, m_b is the wet weight of sample, and ρ is the density of saturation liquid. Table 1 listed the measured porosities of the four NC membranes with different wicking velocities supplied by the manufacturer. For each specification, the weighting experiments were repeated five times with the deviation of the calculated porosity less than 5%.

Pore/particle size distributions. A series of microstructure images of NC membranes were taken using the FEI Quanta 400 scanning electron microscopy (SEM). Since NC membranes were not conductive, sputter coating treatment was performed before SEM imaging. The diameters of gold nanoparticles used in the coating were less than 20 nm [39], while the pore diameters of NC membranes were on the order of 1 μm (Table 1). Therefore, sputter coating should not affect the microstructure images of the present NC membranes.

2.2. Permeability measurements

Theoretical basis of rate-of-rise experiment for porous media. Liquid imbibition in a porous medium such as paper is balanced by capillary, gravitational, viscous and inertial forces.

With evaporation and inertial effects ignored, analytical solutions for capillary wicking flow in horizontal (without gravity) and vertical (with gravity) conditions can be written as [37,40]:

$$h^2 = \frac{4K\sigma}{\varepsilon \mu r_{eff}} t \tag{2}$$

$$\frac{K\rho^2 g^2}{\varepsilon\mu} t + \frac{2\sigma}{r_{eff}} \ln\left(1 - \frac{\rho g r_{eff}}{2\sigma} h\right) + \rho g h = 0 \tag{3}$$

Here, the density ρ, the dynamic viscosity μ, the surface tension σ and the gravitational acceleration g are all constants. r_{eff} ($=r_p/\cos\theta$) is the effective pore radius, where r_p is the equivalent radius of the capillary, and θ is the contact angle between the solid and liquid at the flow front.

Table 1
Statistical results of microstructural parameters of NC membranes.

Specification*	Porosity	Particle size d (μm)	Pore size d_p (μm)	Average d (μm)	Average d_p (μm)
HFC07502	90.5%	1.2-3.9	4.8-14.8	2.061	8.323
HFC09002	87.4%	1.2-4.2	4.0-18.0	2.335	8.885
HFC13502	86.6%	0.8-2.2	1.5-12.0	1.384	4.909
HFC18002	80.9%	0.9-3.3	1.8-9.3	1.759	4.044

* Millipore™, HFC07502, HFC09002, HFC13502 & HFC18002, labelled by nominal capillary flow time, *i.e.*, the seconds required for a liquid to move along and completely fill a strip of 4 cm [24].

The height of liquid uptake h was recorded with capillary time t during experiments. The permeability K and the effective pore radius r_{eff} can then be obtained by fitting the experimental data under the circumstances that the porosity ε has been obtained in Section 2.1.

Experimental setup. To measure the permeability and effective pore radius which are both microstructure dependent, capillary flow experiments for four different NC membranes (Table 1) were designed for tests in both horizontal and vertical positions (Fig. 2).

The experimental setup included a sealed box, a thermo-hygrometer, a digital video camera, and a compact positioning stage. The sealed box was made of polymethylmethacrylate (PMMA), and there was no heat source in it, ensuring the temperature in the box remained almost constant at the room temperature of 25°Cand the humidity above 99% was maintained to avoid evaporation during capillary flow experiments (monitored by the thermo-hygrometer 605-H1, Testo™). The digital video camera (FDR-AX30, SONY™) had a frame rate of 50 fps and a screen resolution of 1920 × 1080. The compact positioning stage was used to gently press the tip of NC membrane into water in the horizontal tests, after which the capillary flow experiment was initiated. The stage was installed on a one-dimensional linear traverse (XSlide, VELMEX™), which was programmable to move with an accuracy of 0.076 mm.

2.3. Permeability modelling

Particle-cubic unit cell model. To model flow transport in a porous medium, accurate representation of its pore geometry is crucial. A close examination of the SEM images suggested that the microstructure of the present NC membrane might be described as a combination of the particle-packing model [19] for granular media such as sintered metal wicks and the cubic model for fibrous media such as highly porous cellular foams [32,33]. Therefore, by replacing cylinders in the cubic cell model with solid spheres (particles), a particle-cubic unit cell model was proposed for NC membranes, as shown in Fig. 3(a), where d and d_p are the particle and pore sizes, respectively. Other assumptions were listed as follows: 1) there was no overlap or gap between adjacent particles; 2) the particles were immovable with fluid flow; 3) the particles were rigid.

To establish a formal relationship among different geometrical parameters characterizing a NC membrane, the particle-cubic unit cell as shown in Fig. 3(a) was analyzed. The volume of the unit cell is:

$$V_{cell} = d_p^3 \tag{4}$$

while the total volume of particles is:

$$V_{particle} = \frac{4}{3}\pi\left(\frac{d}{2}\right)^3 \cdot \left[\left(\frac{d_p}{d} - 1\right) \cdot 12 \cdot \frac{1}{4} + 8 \cdot \frac{1}{8}\right] \tag{5}$$

According to Eq. (1), the porosity of the idealized NC membrane is:

$$\varepsilon = \frac{V_{cell} - V_{particle}}{V_{cell}} \tag{6}$$

Substituting Eqs. (4) and (5) into Eq. (6) yields:

$$\varepsilon = \frac{\pi}{3}\left(\frac{d}{d_p}\right)^3 - \frac{\pi}{2}\left(\frac{d}{d_p}\right)^2 + 1 \tag{7}$$

Equation (7) shows that the microstructural parameters (i.e., porosity, particle size and pore size) are not independent: the porosity is a function of particle to pore size ratio. The inverse correlation of Eq. (7) is:

$$\frac{d}{d_p} = \phi(\varepsilon) \tag{8}$$

with

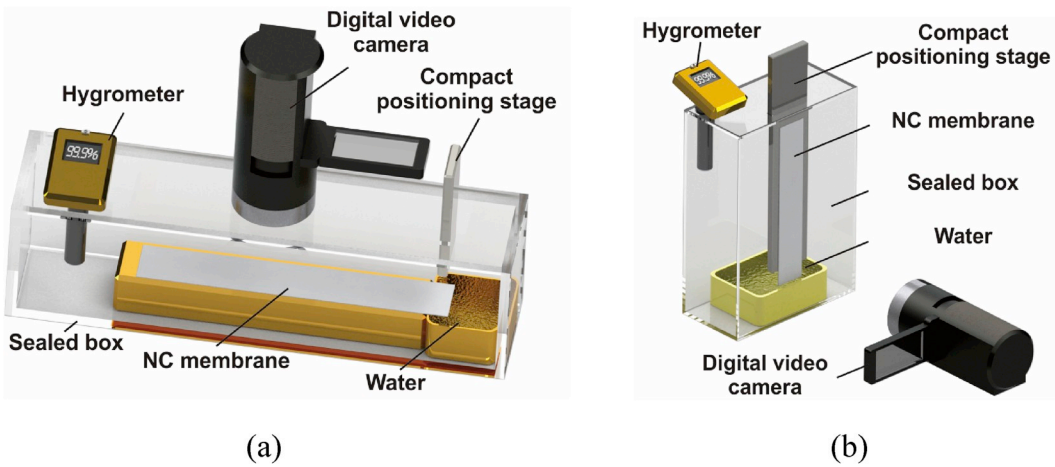

Fig. 2. Rate-of-rise experimental setup: (a) horizontal test; (b) vertical test.

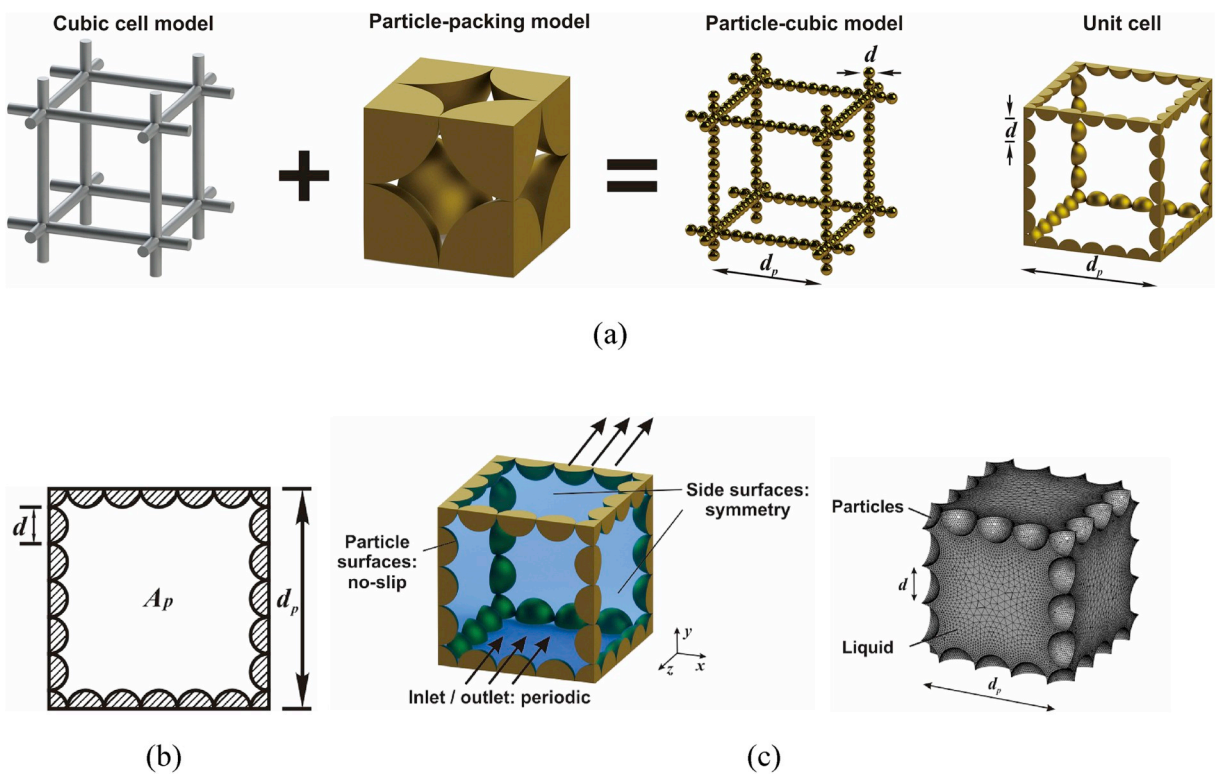

Fig. 3. Permeability modelling methods. (a) Unit cell geometrical model; (b) Projection of the particle-cubic unit cell along the orthogonal axis; (c) computational domain and mesh.

$$\phi(\varepsilon) = \frac{1}{2} + \cos\left\{\frac{1}{3}\left[\pi + \arccos\left(\frac{12}{\pi}(1-\varepsilon) - 1\right)\right]\right\} \tag{9}$$

Numerical model. Fig. 3(c) displayed the unit cell model and boundary conditions used in numerical simulations to calculate the permeability of NC membrane. A multi-block unstructured mesh incorporating fully tetrahedral elements was generated in Gambit 2.4.6, as shown in Fig. 3(c). To capture the flow and thermal boundary layers, a size function was employed to refine the local mesh around solid-fluid interfaces.

To simplify the numerical problem, the following assumptions were made: 1) the flow was three-dimensional steady-state laminar Darcy flow; 2) the physical properties of water were constant; 3) the flow process did not involve temperature changes. Correspondingly, the governing equations of the numerical model were expressed as below.

Continuity equation:

$$\nabla \cdot (\rho \mathbf{v}) = 0 \tag{10}$$

Momentum equation:

$$\rho \frac{D\mathbf{v}}{Dt} = -\nabla p + \mu \nabla^2 \mathbf{v} \tag{11}$$

where ρ and μ are the density and viscosity of water, respectively.

A commercial CFD (computational fluid dynamics) code (ANSYS Fluent 14.5) was employed to solve the problem as formulated. The SIMPLE algorithm was applied to couple the pressure and velocity for numerical analysis [41–43]. A second-order upwind scheme was applied to discretize the convective terms of the governing equations. The iterative convergence criterion was chosen as 10^{-3} for momentum

equation. For selected cases, this was verified to be small enough to ensure the predicted results were independent of the chosen values. To check grid independency, the number of elements was systematically increased from 0.4 million to 2 million: the results showed no difference as the grid number was varied.

Non-slip boundary conditions were applied on the particle surfaces. Periodic boundary conditions were imposed on the external surfaces of the computational domain. Pressure gradient was specified across the inlet/outlet boundaries. Volumetric flow rate along the flow direction was calculated from the numerical simulation. Then the permeability was calculated according to the Darcy's law, as:

$$K = -\frac{\mu Q}{A}\cdot\frac{dx}{dP} = -\frac{\mu Q}{d_p^2}\cdot\frac{d_p}{\Delta P} = -\frac{\mu Q}{d_p \Delta P} \tag{12}$$

where Q is the volumetric flow rate and ΔP is the pressure difference between the inlet and outlet.

Theoretical model. Using the cubic cell model of Fig. 3(a), Plessis et al. [44] developed an analytical expression of permeability for high porosity cellular metal foams, as:

$$K = \frac{\varepsilon}{108(\chi - 1)} d_p^2 \tag{13}$$

where χ is the tortuosity of fluid flow across the porous solid matrix. The tortuosity of the porous matrix is defined as the quotient of the total winding path length (which is available within the representative cubic cell for flow under a constant cross-section A) and the basic streamwise dimension of the porous medium microstructure [44]. In short, the tortuosity is the ratio of the path that the flow actually travels to the theoretical shortest path through the porous medium, which represents the resistance of fluid flowing through the porous medium smoothly.

According to Plessis et al. [44], the tortuosity χ of the cubic cell model is:

$$\chi = \frac{\varepsilon d_p^2}{A_p} \tag{14}$$

where A_p is the cross-sectional area of the pore in a porous medium. Given that the tortuosity χ could also be expressed as $\chi = V_f/(d_p A_p)$, V_f being the void part of the cubit cell [45], when $\chi = 1$ (*i.e.*, $V_f = d_p A_p$) the cubic cell would become a cavity without solid obstruction, *i.e.*, the fluid channel becomes an empty one. In this case, there was no obstruction to the flow and the permeability became infinite [44], as indicated by Eq. (13) when the tortuosity approached a value of one. For the particle-cubic unit cell model as shown in Fig. 3(a), A_p should be modified by projecting it along the orthogonal axis (referred to Fig. 3 (b)), as:

$$A_p = d_p^2 - \pi\left(\frac{d}{2}\right)^2\left[\left(\frac{d_p}{d} - 1\right)\cdot 4\cdot\frac{1}{2} + 1\right] = d_p^2 - \frac{\pi}{2} d d_p + \frac{\pi}{4} d^2 \tag{15}$$

Substituting (15) into (14) yields:

$$\chi = \frac{\varepsilon}{1 - \frac{\pi}{2}\cdot\frac{d}{d_p} + \frac{\pi}{4}\left(\frac{d}{d_p}\right)^2} \tag{16}$$

Finally, upon substituting further (9) and (16) into (13), the permeability of the proposed particle-cubic unit cell model was obtained as:

$$\frac{K}{d_p^2} = \frac{\varepsilon}{108\left\{\frac{\varepsilon}{1 - \frac{\pi}{2}\cdot\phi(\varepsilon) + \frac{\pi}{4}[\phi(\varepsilon)]^2} - 1\right\}} \tag{17}$$

3. Results and discussion

3.1. Pore-structure characterization

To characterize the pore-structure, we obtained the SEM images of four NC membranes with different specifications, e.g., HFC07502, HFC09002, HFC13502 & HFC18002 from Millipore™. We also measured their porosity using the weighting method as mentioned in Section 2.1. As shown in Fig. 4(a–d), the NC membranes exhibited cross-linked and granular microstructures. The pore size decreased from HFC07502 to HFC18002, while the particle sizes were almost the same. In order to determine the exact value of relevant microstructural parameters, for each specification, about 500 data points of particle size and pore size were extracted from SEM images. Fig. 4(e–l) showed the pore/particle size distributions, while Table 1 listed the corresponding statistically averaged pore/particle sizes.

As shown in Fig. 4(e–l), the particle size exhibited the Gauss distribution while the pore size distribution was closer to the skewed distribution. The particle size of HFC18002 showed an exceptional skewed distribution compared to the normal distribution in the remaining membranes, which may be caused by the larger statistical error for HFC18002 membrane: it had the lowest porosity, with particles lumped together as shown in the SEM image. However, there was no doubt that the unevenness of pore sizes was more obvious than that of particle sizes. In addition, while the four specifications had similar average particle sizes, their average pore sizes and porosities were obviously different. This was consistent with that visually observed from the SEM images and the experimentally measured average pore radius given in Table 1.

Before we can model the microscale flow in porous materials at the pore level, a geometrical model representing the major features of the pore morphology should be developed. To this end, we proposed a particle-cubic unit model for NC membrane, based on which the theoretical relation among geometrical parameters had been derived. As shown in Eq. (7), the parameters characterizing pore structure, i.e., particle size d, pore size d_p and porosity ε, are not independent. On the contrary, the porosity is only a function of particle to pore size ratio. For comparison, the theoretical curve of Eq. (7) and the experimental data of Table 1 were plotted together in Fig. 5. Relatively good agreement was achieved. Errors of porosities for different specifications were 1.61%, 4.18%, 3.26% and 2.00%, respectively, suggesting that the idealized particle-cubic model is adequate in representing the pore geometry of the present NC membranes.

3.2. Microstructural effects on the wicking flow behavior

In order to relate the microstructure with the wicking flow behavior, we measured the wicking flow dynamics of four NC membranes having different specifications, with each specification repeated five times. For NC membranes of the same specification in the same condition, the data points overlapped with each other for different samples (maximum deviation less than 2%). A typical sequence of imbibition pictures for the four NC membranes (HFC07502, HFC09002, HFC13502 and HFC18002) was displayed in Fig. 6(a), which showed that the capillary flow speed was fast during the initial stage and then gradually decreased. Typical data of uptake height plotted as a function of capillary time from HFC07502 to HFC18002 were presented in Fig. 6(b) and (c) for horizontal and vertical tests, respectively, showing that the wicking speed decreased from HFC07502 to HFC18002. The height of water uptake and the capillary flow time satisfied the power relationship of 1/2 in line with the Washburn equation (Eq. (2)). Volume change of these NC membranes was not obvious so that swelling effect may be ignored.

Based on the experimentally measured uptake height versus capillary time curves, the permeability and effective pore radius could be fitted according the theoretical solutions given in Eqs. (2) and (3). Table 2 listed the results for the present NC membranes, showing that

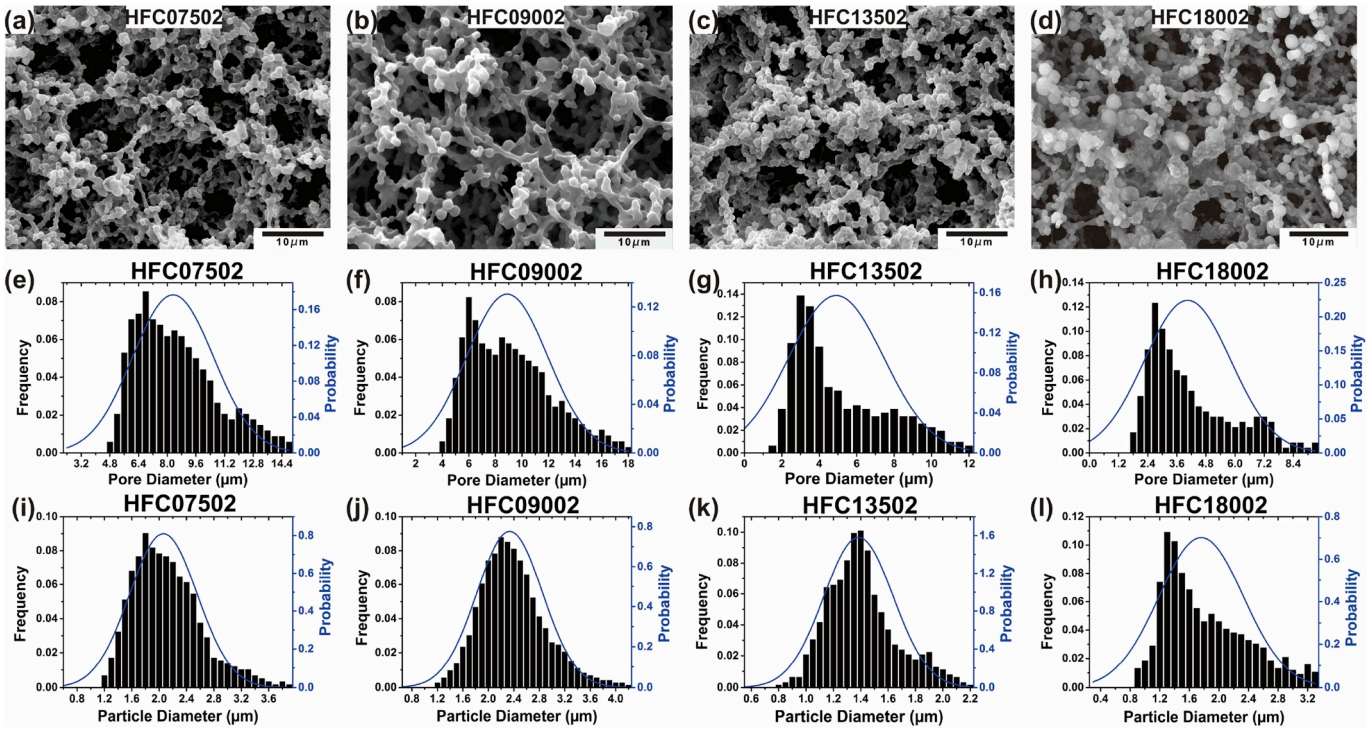

Fig. 4. Microstructure characterization. (a–d) SEM images of NC membranes; (e–h) frequency histogram of pore diameter of NC membranes; (i–l) frequency histogram of particle diameter of NC membranes.

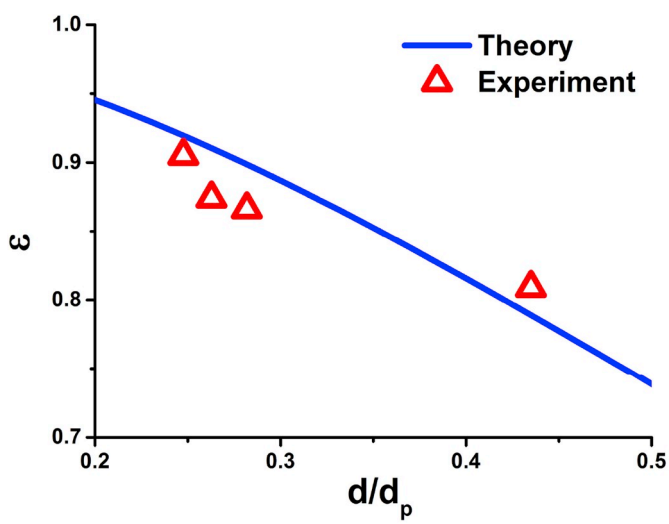

Fig. 5. Porosity plotted as a function of particle to pore size ratio: model predictions versus experimental measurements.

the both the effective pore radius and permeability decreased from HFC07502 to HFC18002.

It can be seen from the SEM images (Fig. 4) that from HFC07502 to HFC18002, the particle arrangement became more and more crowded and dense, and the degree of stacking was gradually increased. Given the average particle size almost constant, a denser stacking of the particles, led to a smaller pore size, a lower porosity and a higher particle/pore size ratio. Both the measured wicking velocity (Fig. 6) and permeability (Table 2) decreased from HFC07502 to HFC18002, which can be attributed to the decreased pore size and porosity (Table 1). The effective pore radius (Table 2), an equivalent pore size obtained based on the capillary model, had an order of magnitude ~ O (10 μm), similar to that of the measured physical pore diameters (Table 1), although their actual values were different.

3.3. Comparison of different permeability models

We have obtained the permeability of four NC membranes with different microstructural parameters using experimental, numerical, and theoretical approaches separately. Fig. 7 compared the present theoretical, experimental and numerical results of NC membrane permeability. As indicated by the theoretical relation of Eq. (17), the dimensionless permeability is only a function of porosity. It was seen that the maximum deviation of our experimental, numerical and theoretical results was less than 5%, thus further validating the present particle-cubic model and theoretical permeability model.

In addition to the particle-cubic model proposed in the present study, there exist other pore-structure based models for the permeability of porous media. Calmidi [32] proposed a cubic cell model for foam matrix and developed an empirical formula to calculate the permeability, as:

$$\frac{K}{d_p^2} = C(1-\varepsilon)^m \left(\frac{d_f}{d_p}\right)^n \tag{18}$$

where $C = 0.00073$, $m = -0.224$, $n = -1.11$, and the ratio of fiber diameter to pore size is:

$$\frac{d_f}{d_p} = 2\sqrt{\frac{1-\varepsilon}{3\pi}}\cdot\frac{1}{G} \tag{19}$$

$$G = 1 - e^{-\frac{1-\varepsilon}{0.04}} \tag{20}$$

Yang et al. [46] adopted the theoretical model of Beeckman [47] for the tortuosity of foam matrix and modified the permeability formula of Eq. (18) as:

$$\frac{K}{d_p^2} = \frac{\varepsilon\left[1-(1-\varepsilon)^{1/3}\right]}{108\left[(1-\varepsilon)^{1/3}-(1-\varepsilon)\right]} \tag{21}$$

Yang et al. [46] demonstrated that the modified formula unified the

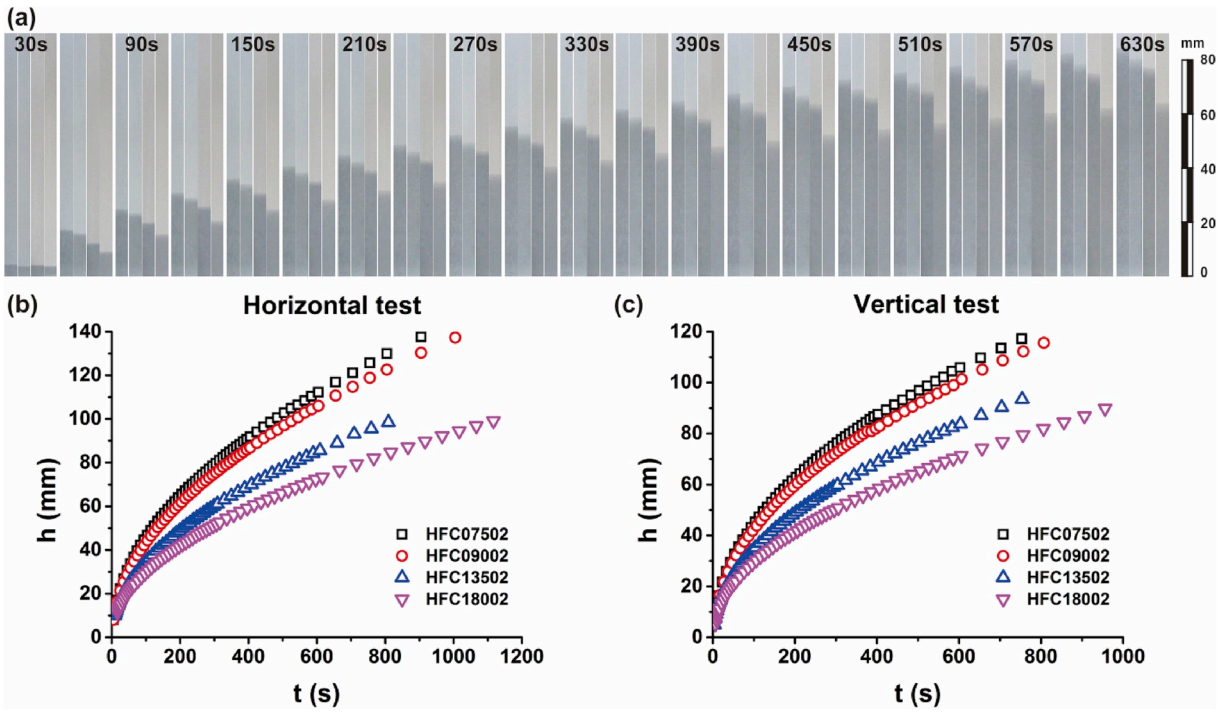

Fig. 6. (a) Typical sequence of imbibition obtained during an experimental run with four different NC membranes (horizontal test). The interval between consecutive pictures was 30 s. From left to right, the images in each group corresponded to HFC07502, HFC09002, HFC13502 and HFC18002; (b–c) height of water uptake plotted as a function of capillary flow time for four different NC membranes in horizontal and vertical positions, respectively.

Table 2
Fitting results of effective pore radius and permeability of selected NC membranes.

Specification*	Effective pore radius r_{eff} (μm)	Permeability K (μm^2)
HFC07502	24.303	1.427
HFC09002	24.283	1.238
HFC13502	13.170	0.428
HFC18002	10.107	0.220

* Millipore^{TM}, HFC07502, HFC09002, HFC13502 & HFC18002, labelled by nominal capillary flow time, *i.e.*, the seconds required for a liquid to move along and completely fill a strip of 4 cm [24].

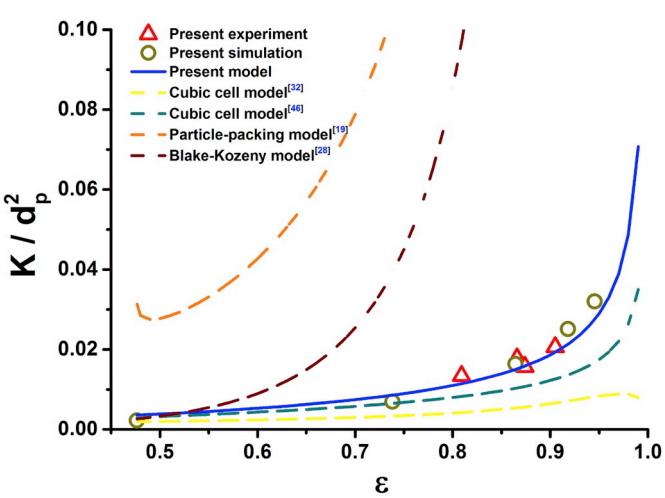

Fig. 7. Dimensionless permeability plotted as a function of porosity: comparison among different theoretical models and the present numerical/experimental results.

previously reported data over a wide range of porosities and pore sizes.

Byon et al. [19] proposed a particle-packing model for sintered metal wicks and obtained a permeability formula based on numerical simulations, as:

$$\frac{K}{d_p^2} = \frac{\varepsilon^3}{150(1-\varepsilon)^2}\left[1 + 4.03\exp\left(3.29\frac{d}{d_p}\right)\left(\frac{d}{d_p}\right)^2\right] \tag{22}$$

Finally, the Blake-Kozeny equation [28] widely used to calculate the permeability of granular porous media was given by:

$$\frac{K}{d_p^2} = \frac{\varepsilon^3}{150(1-\varepsilon)^2} \tag{23}$$

As shown in Fig. 7, for the present NC membranes, existing correlations based on the cubic cell model and the particle-packing model induced significant deviations compared to our experimental results. The cubic cell model was developed for the matrix type of porous materials such as metal foams with high porosities (>0.9), whereas the particle-packing model was applicable for granular porous material having relatively low porosities (<0.5). Typically, the pore geometry of a NC membrane (having a porosity between 0.7-0.9) can't be regarded as the matrix or granular, but is close to a combination of the two. Therefore, existing correlations are not applicable to NC membranes with unique pore structures, and it is necessary to adopt the particle-cubic cell model to simulate flow transport in NC membranes more accurately. Our geometrical model and theoretical permeability model will be useful tools in tailoring the capillary flow behavior of NC membranes by controlling the microstructural parameters, and optimizing the NC-based biomedical devices from the view point of material design in the future.

4. Conclusions

The effects of pore morphology on capillary flow properties with a focus on the permeability of NC membranes were investigated using a combined experimental, theoretical and numerical approach. For

selected NC membranes with different specifications, their microstructural parameters such as particle/pore size and porosity were measured and characterized. Then the capillary flow properties (e.g., permeability and effective pore radius) were measured using the rate-of-rise experiment. A microstructural geometry model (termed the particle-cubic unit cell model) was proposed to represent the pore structure of the NC membrane. The porosity thus predicted depends only upon the particle to pore size ratio, which was validated by experimentally measured pore geometry data. Based on the particle-cubic model, numerical simulations were also performed to calculate the permeability. In addition, a closed-form solution of the permeability was obtained by quantifying the tortuosity of the particle-cubic model. Results from the rate-of-rise experiment, numerical simulation, and closed-form solution collapsed on a single curve. It was found that the microstructure of NC membrane greatly affects the capillary flow behavior: with the particle size almost constant, the denser stacking of the particles leads to a smaller pore size, a lower porosity, and a higher particle/pore size ratio, thus yielding lower capillary wicking velocity and lower flow permeability. Finally, it was demonstrated that existing theoretical models of permeability for matrix foam and granular porous media are not applicable to NC membranes as the latter exhibit a unique pore structure. The particle-cubic model as developed in the present study appeared to capture well the behavior of fluid flow across the NC membranes. In the future, to further improve the model, capillary flow properties integrating reactive transport need to be considered for various biomedical applications.

Author contributions

Shanyouming Sun: Designing experiments, drafting the article, data analysis and interpretation. **Shangsheng Feng:** Critical revision of the article, designing the work. **Changchun Ji:** Experiment assistant. **Meng Shi:** Data collection. **Xiaocong He:** Data collection. **Feng Xu:** Critical revision of the article. **Tian Jian Lu:** Designing the work, critical revision of the article.

Acknowledgment

This work was supported by the National Natural Science Foundation of China (51676156), the National 111 Project of China (B06024), the Postdoctoral Science Foundation of China (2016M590942), the Shaanxi Province Science Foundation, and the Fundamental Research Funds for the Central Universities in China.

References

[1] G.E. Fridley, C.A. Holstein, S.B. Oza, P. Yager, The evolution of nitrocellulose as a material for bioassays, Mater. Res. Bull. 38 (2013) 326–330.
[2] R.C. Wong, H.Y. Tse, Lateral Flow Immunoassay, Humana Press, New York, 2009, pp. 95–113.
[3] J. Hu, S.Q. Wang, L. Wang, F. Li, B. Pingguan-Murphy, T.J. Lu, F. Xu, Advances in paper-based point-of-care diagnostics, Biosens. Bioelectron. 54 (2014) 585–597.
[4] T.M. Squires, R.J. Messinger, S.R. Manalis, Making it stick: convection, reaction and diffusion in surface-based biosensors, Nat. Biotechnol. 26 (2008) 417–426.
[5] Z. Liu, J. Hu, A. Li, S. Feng, Z. Qu, F. Xu, The effect of report particle properties on lateral flow assays: a mathematical model, Sens. Actuators B Chem. 248 (2017) 699–707.
[6] E. Elizalde, R. Urteaga, C.L.A. Berli, Rational design of capillary-driven flows for paper-based microfluidics, Lab Chip 15 (2015) 2173–2180.
[7] E. Fu, S.A. Ramsey, P. Kauffman, B. Lutz, P. Yager, Transport in two-dimensional paper networks, Microfluid. Nanofluidics 10 (2011) 29–35.
[8] P. Kauffman, E. Fu, B. Lutz, P. Yager, Visualization and measurement of flow in two-dimensional paper networks, Lab Chip 10 (2010) 2614–2617.
[9] J.L. Osborn, B. Lutz, E. Fu, P. Kauffman, D.Y. Stevens, P. Yager, Microfluidics without pumps: reinventing the T-sensor and H-filter in paper networks, Lab Chip 10 (2010) 2659–2665.
[10] Z. Liu, J. Hu, Y. Zhao, Z. Qu, F. Xu, Experimental and numerical studies on liquid wicking into filter papers for paper-based diagnostics, Appl. Therm. Eng. 88 (2015) 280–287.
[11] S. Hong, W. Kim, Dynamics of water imbibition through paper channels with wax boundaries, Microfluid. Nanofluidics 19 (2015) 845–853.
[12] L. Rivas, M. Medina-Sánchez, A. Escosura-Muñiz, A. Merkoçi, Improving sensitivity of gold nanoparticle-based lateral flow assays by using wax-printed pillars as delay barriers of microfluidics, Lab Chip 14 (2014) 4406–4414.
[13] C. Parolo, M. Medina-Sanchez, A. Escosura-Muniza, A. Merkoci, Simple paper architecture modifications lead to enhanced sensitivity in nanoparticle based lateral flow immunoassays, Lab Chip 13 (2013) 386–390.
[14] S. Jahanshahi-Anbuhi, A. Henry, V. Leung, C. Sicard, K. Pennings, R. Pelton, J. D. Brennan, C.D.M. Filipe, Paper-based microfluidics with an erodible polymeric bridge giving controlled release and timed flow shutoff, Lab Chip 14 (2014) 229–236.
[15] X. Li, P. Zwanenburg, X. Liu, Magnetic timing valves for fluid control in paper-based microfluidics, Lab Chip 13 (2013) 2609–2614.
[16] A. Böhm, M. Biesalski, Paper-based microfluidic devices: a complex low-cost material in high-tech applications, MRS Bull. 42 (2017) 356–364.
[17] K. Chaudhury, S. Kar, S. Chakraborty, Diffusive dynamics on paper matrix, Appl. Phys. Lett. 109 (2016) 224101.
[18] A. Böhm, F. Carstens, C. Trieb, S. Schabel, M. Biesalski, Engineering microfluidic papers: effect of fiber source and paper sheet properties on capillary-driven fluid flow, Microfluid. Nanofluidics 16 (2014) 789–799.
[19] C. Byon, S.J. Kim, Capillary performance of bi-porous sintered metal wicks, Int. J. Heat Mass Transf. 55 (2012) 4096–4103.
[20] A. Kopanidis, A. Theodorakakos, E. Gavaises, D. Bouris, 3D numerical simulation of flow and conjugate heat transfer through a pore scale model of high porosity open cell metal foam, Int. J. Heat Mass Transf. 53 (2010) 2539–2550.
[21] A.L. Ahmad, S.C. Low, S.R.A. Shukor, W.J.N. Fernando, A. Ismail, Hindered diffusion in lateral flow nitrocellulose membrane: experimental and modeling studies, J. Membr. Sci. 357 (2010) 178–184.
[22] G.D. Wehinger, T. Eppinger, M. Kraume, Detailed numerical simulations of catalytic fixed-bed reactors: heterogeneous dry reforming of methane, Chem. Eng. Sci. 122 (2015) 197–209.
[23] J. Rickenbach, F. Lucci, P.D. Eggenschwiler, D. Poulikakos, Pore scale modeling of cold-start emissions in foam based catalytic reactors, Chem. Eng. Sci. 138 (2015) 446–456.
[24] Rapid Lateral Flow Test Strips: Considerations for Product Development, 2013. www.merckmillipore.com/diagnostics.
[25] M. Janko, M. Jocher, A. Boehm, L. Babel, S. Bump, M. Biesalski, T. Meckel, R. W. Stark, Cross-linking cellulosic fibers with photoreactive polymers: visualization with confocal Raman and fluorescence microscopy, Biomacromolecules 16 (2015) 2179–2187.
[26] S. Bump, A. Böhm, L. Babel, S. Wendenburg, F. Carstens, S. Schabel, M. Biesalski, T. Meckel, Spatial, spectral, radiometric, and temporal analysis of polymer-modified paper substrates using fluorescence microscopy, Cellulose 22 (2015) 73–88.
[27] C. Zhang, J.W. Palko, G. Rong, K.S. Pringle, M.T. Barako, T.J. Dusseault, M. Asheghi, J.G. Santiago, K.E. Goodson, Tailoring permeability of microporous copper structures through template sintering, ACS Appl. Mater. Inter. 10 (2018) 30487–30494.
[28] J. Kozeny, Ueber kapillare leitung des wassers im boden, Sitz. ber. Akad. Wiss. Wien 136 (1927) 271–306.
[29] C. Byon, S.J. Kim, The effect of the particle size distribution and packing structure on the permeability of sintered porous wicks, Int. J. Heat Mass Transf. 61 (2013) 499–504.
[30] I.L. Ngo, C. Byon, Permeability of microporous wicks with geometric inverse to sintered particles, Int. J. Heat Mass Transf. 92 (2016) 298–302.
[31] W. Thomson, On the division of space with minimum partitional area, Philos. Mag. 24 (1887) 503.
[32] V.V. Calmidi, Transport Phenomena in High Porosity Fibrous Metal Foams, Ph.D. Thesis, University of Colorado, 1998.
[33] T.J. Lu, H.A. Stone, M.F. Ashby, Heat transfer in open-cell metal foams, Acta Mater. 46 (1998) 3619–3635.
[34] D. Weaire, R. Phelan, A counter-example to Kelvin's conjecture on minimal surfaces, Philos. Mag. Lett. 69 (1994) 107–110.
[35] H. Giesche, Mercury porosimetry: a general (practical) overview, Part. Part. Syst. Char. 23 (2006) 9–19.
[36] K. Sing, The use of nitrogen adsorption for the characterization of porous materials, Colloids Surf., A 187 (2001) 3–9.
[37] B. Holley, A. Faghri, Permeability and effective pore radius measurements for heat pipe and fuel cell applications, Appl. Therm. Eng. 26 (2006) 448–462.
[38] M. Kruk, Z. Li, M. Jaroniec, W.R. Betz, Nitrogen adsorption study of surface properties of graphitized carbon blacks, Langmuir 15 (1999) 1435–1441.
[39] M.C. Daniel, D. Astruc, Gold nanoparticles: assembly, supramolecular chemistry, quantum-size-related properties, and applications toward biology, catalysis, and nanotechnology, Chem. Rev. 104 (2004) 293–346.
[40] E.W. Washburn, The dynamics of capillary flow, Phys. Rev. 17 (1921) 273–283.
[41] S.S. Feng, S.Y.M. Sun, H.B. Yan, M. Shi, T.J. Lu, Optimum composition of gas mixture in a novel chimney-based LED bulb, Int. J. Heat Mass Transf. 115 (2017) 32–42.
[42] S.S. Feng, J.J. Kuang, T. Wen, T.J. Lu, K. Ichimiya, An experimental and numerical study of finned metal foam heat sinks under impinging air jet cooling, Int. J. Heat Mass Transf. 77 (2014) 1063–1074.
[43] J. Hu, S. Lv, S. Feng, M. Long, Flow dynamics analyses of pathophysiological liver lobules using porous media theory, Acta Mech. Sin. 33 (4) (2017) 823–832.
[44] P.D. Plessis, A. Montillet, J. Comiti, J. Legrand, Pressure drop prediction for flow through high porosity metallic foams, Chem. Eng. Sci. 49 (1994) 3545–3553.
[45] J.G. Fouriea, J.P. DuPlessis, Pressure drop modelling in cellular metallic foams, Chem. Eng. Sci. 57 (2002) 2781–2789.

[46] X.H. Yang, T.J. Lu, T. Kim, An analytical model for permeability of isotropic porous media, Phys. Lett. A 378 (2014) 2308–2311.
[47] J.W. Beekman, Mathematical description of heterogeneous materials, Chem. Eng. Sci. 45 (1990) 2603–2610.
[48] P.X. Jiang, R.N. Xu, W. Gong, Particle-to-fluid heat transfer coefficients in miniporous media, Chem. Eng. Sci. 61 (2006) 7213–7222.